ANNALS OF GEOPHYSICS, 68, 4, A449, 2025; doi:10.4401/ag-9289
OPEN ACCESS

Unusual vertical oscillations in sodium density and the formation of sporadic sodium layer over the Zhongshan station

Alicreance Hiyadutuje[*,1], Xiangcai Chen[2,3,4], John Bosco Habarulema[1,5,6], Michael J. Kosch[1,7,8], Judy A. E. Stephenson[7], Tshimangadzo Merline Matamba[1,5], Wentao Huang[2,3,4], Chao Ban[9,10]

(1) South African National Space Agency (SANSA), Hermanus, South Africa
(2) MNR Key Laboratory for Polar Science, Polar Research Institute of China (PRIC), Shanghai, China
(3) Antarctic Zhongshan Ice and Space Environment National Observation and Research Station, Polar Research Institute of China (PRIC), Shanghai, China
(4) State Key Laboratory of Lunar and Planetary Sciences, Macau University of Science and Technology (MUST), Macau, China
(5) Department of Physics and Electronics, Rhodes University (RU), Makhanda, South Africa
(6) Centre for Space Research, North-West University (NWU), Potchefstroom , South Africa
(7) Department of Chemistry and Physics, University of KwaZulu Natal (UKZN), Durban, South Africa
(8) Department of Physics, University of Lancaster (UL), UK
(9) State Key Laboratory of Atmospheric Environment and Extreme Meteorology, Institute of Atmospheric Physics, Chinese Academy of Sciences (CAS), Beijing, China
(10) Laboratory of Middle Atmosphere and Global Environment Observation, Institute of Atmospheric Physics, Chinese Academy of Sciences (CAS), Beijing, China

Article history: received February 14, 2025; accepted June 28, 2025

Abstract

Unusual vertical oscillations with some wave structures were observed in the sodium (Na) density layers (SLs) in Antarctica on 1 September 2019, by means of the lidar located at Zhongshan (69°S, 76°E). There was a clear vertical convection of the wavy sodium density layers which populated the region at an altitude of between ~90 and ~102 km producing the Sporadic/Sudden Sodium Layers (SSLs). The vertical oscillations had an average wavelength, average speed and period of ~3.0-4.5 km, ~7.8 m/s and ~7.3-8.5 min, respectively. The possible cause of these vertical oscillations, as well as the mechanisms that could be behind the generation of these oscillations and wavy SSLs, were investigated. The Global Positioning System (GPS) satellite receiver located at Davis (68.6°S, 77.9°E), 116 km away from Zhongshan, was used to derive the Total Electron Content (TEC) perturbations in the region surrounding Zhongshan. SuperDARN HF radar at Zhongshan also showed some waves in the first 10 range gates (180-800 km away), suggesting that the Traveling Ionospheric Disturbances (TIDs) were propagating in the *E*-region. The cross-correlation between GPS and lidar wave structures was computed. A good to strong correlation of –0.6-–0.9 was found between waves observed by GPS and lidar. Additionally, a moderate correlation was found between the SuperDARN radar and lidar wave structures. The lidar neutral temperature showed upward Atmospheric Gravity Waves (AGWs), while SuperDARN and GPS showed the downward TIDs. Based on the polar cap (PC) index, TIDs could have been generated by Joule heating due to geomagnetic storm effects in the region. The estimated Richardson number values between 80 and 105 km at 16:00-24:00 UT suggest that convective and dynamic instabilities could have generated the observed SSLs and AGWs. Vertical oscillation of the sodium density layers could have taken place because of waves breaking and interference from the downward TIDs and upward AGWs.

Keywords: Vertical oscillations; SSL; Convective and dynamic instabilities; AGWs and TIDs; Neutral wind; Neutral temperature

---

1. Introduction

Sodium density Layers (SLs) are formed by means of physical and chemical processes (Plane et al., 2015). Sodium (Na) atoms and Na^+ ions are absorbed in atmospheric dust, smoke particles, energetic auroral particles (Von Zahn et al., 1987; Heinselman et al., 1998) and Na from the meteor ablation (Swenson and Gardner, 1998). The SLs develop in the lower part of the ionospheric *E*-region where most space weather phenomena are coupled with other phenomena resulting from terrestrial weather. This coupling between space and terrestrial weather is governed by the momentum and energy exchange between internal waves, such as the Atmospheric Gravity Waves (AGWs) and tides, Sudden Stratospheric Warmings (SSWs), and solar activity events such as solar irradiance, solar wind, solar flares, and Coronal Mass Ejections (CMEs) (Avakyan, 2008; Yiğit et al., 2016). This momentum and energy exchange between the two systems is not well understood, especially within the Earth's stratosphere, mesosphere and thermosphere (Qiu et al., 2021). SLs variations and Sudden or Sporadic Sodium Layers (SSLs) during different geomagnetic conditions have been reported in the past. For example, Yuan et al. (2025) found that Na number density above an altitude of 105 km in the mid-latitude was depleted during a geomagnetic storm likely through the vertical heat advection and adiabatic processes. Takahashi et al. (2015) demonstrated that the SSL was caused mainly by the sodium ions from the Na number density layers by means of the electric field during low background temperatures at high latitudes. Es-layer and auroral particle precipitation also would have contributed to the SSL generation to some extent. Heinselman et al. (1998) found that the sodium number density decreases during the aurora, but it is generated by the Es-layer. A review paper about the SSL was published by Qiu et al. (2016). It highlights most of the abovementioned mechanisms responsible for the SSL. Yu et al., (2017) reported that thunderstorms can enhance the Na number density. There are other studies that report the propagation of AGWs through the Na density layers (Shelton et al. 1980; Gardner and Shelton, 1985; Kirkwood, 1989; Sato, 1992).

The AGWs generated in the lower part of the atmosphere transport energy and momentum to the upper atmosphere and sometimes break at the mesopause to generate secondary waves with short periods that lose some of their energy to the medium (Hecht et al., 2000; Snively and Pasko, 2003). AGWs have proven to contribute to the considerable variations in SLs and SSLs (Cai et al., 2017). On the other hand, the waves caused by heating or by the Lorentz force in the ionosphere may propagate downward from the thermosphere during geomagnetic activity (Richmond, 1978; Hocke et al., 1996). Waves propagating in the thermosphere take different names such as AGWs (Roble et al., 1978; Richmond, 1979; Hocke et al., 1996), Thermospheric Gravity Waves (TGWs), Traveling Atmospheric Disturbances (TADs) (Bruinsma and Forbes, 2007, 2009) and Traveling Ionospheric Disturbances (TIDs) (Hocke et al., 1996). In this study, the waves generated in the auroral zone of the ionospheric high latitudes are referred to as TADs/TIDs. TIDs are wavelike perturbations of the ionospheric plasma or simply the manifestations of the AGWs (Munro, 1950; Hunsucker, 1982; Hocke et al., 1996; Shinbori et al., 2022). AGWs can be observed directly using interferometer, satellite mass spectrometer/accelerometer, airglow imager, and lidars (Nomura et al., 1987; Hocke et al., 1996; Hecht et al., 2001). AGWs can be observed indirectly as the TIDs using radio techniques (Hocke et al., 1996). There are other mechanisms that could be responsible for the generation of TIDs, such as Joule heating, the Perkins instability and the Lorentz force (Cherniak and Zakharenkova, 2018b; Hiyadutuje et al., 2022). The TIDs generated by AGWs would have the same scales (Hunsucker, 1982) as Large (L), Medium (M) and Small (S), and can also generate variations in SLs. TIDs are observed by radio techniques such as incoherent scatter radars, HF Doppler, ionosondes or Global Positioning System (GPS) satellites (Williams et al., 1988; Hocke et al., 1996). Both types of waves are observed in the lower part of the ionospheric *E*-region where the SLs are formed at altitudes between 80 and 110 km.

In this study, Na number density vertical oscillation and the formation of SSLs at Zhongshan in Antarctica are reported. Vertical oscillating wavy SLs and SSLs were observed using the recently installed sodium lidar. TIDs, AGWs and instabilities were observed on 1 September 2019 and were considered as the contributing mechanisms. The Zhongshan Super Dual Auroral Radar Network known as SuperDARN High Frequency (HF) radar (Greenwald et al., 1995; Chisham et al., 2007), the lidar located at 69°S, 76°E, and GPS receiver (Liu et al., 1996; Ding et al., 2007) at Davis station (68.6°S, 77.9°E) were used to observe the TIDs/TADs.

2. Instruments and Methods

2.1 Zhongshan Na Lidar

The lidar at Zhongshan was installed in 2019 to measure the sodium density, horizontal neutral wind, and temperature in the lower part of the *E*-region (Chen et al., 2021). The three-frequency sodium resonance fluorescence Doppler lidar has a transmitter, receiver, data acquisition and system control modules (Krueger et al., 2015). It transmits pulses in four stages using a dye amplifier that has a 589 nm frequency-doubled solid state diode laser. Photons are received from 3 directions using three 82 cm diameter microcrystal-glass subtrate parabolic telescopes. The first, second and third telescopes are at zenith, 30° from the zenith to the south and 30° from the zenith to the west, respectively, to measure the wind (Chen et al., 2021). It transmits 0.55 W in each direction and photons are detected by photomultiplier tubes with a time and spatial resolution of 15 s and 45 m, respectively. The data were smoothed by averaging the data points within 1 km and a 25 min rolling window. Linear detrending was done before computing the period. The period of TADs was computed by means of the autocorrelation (https://pandas.pydata.org/docs/reference/api/pandas.plotting.autocorrelation_plot.html). Figure 1 shows the Zhongshan station (black dot) where the lidar was installed.

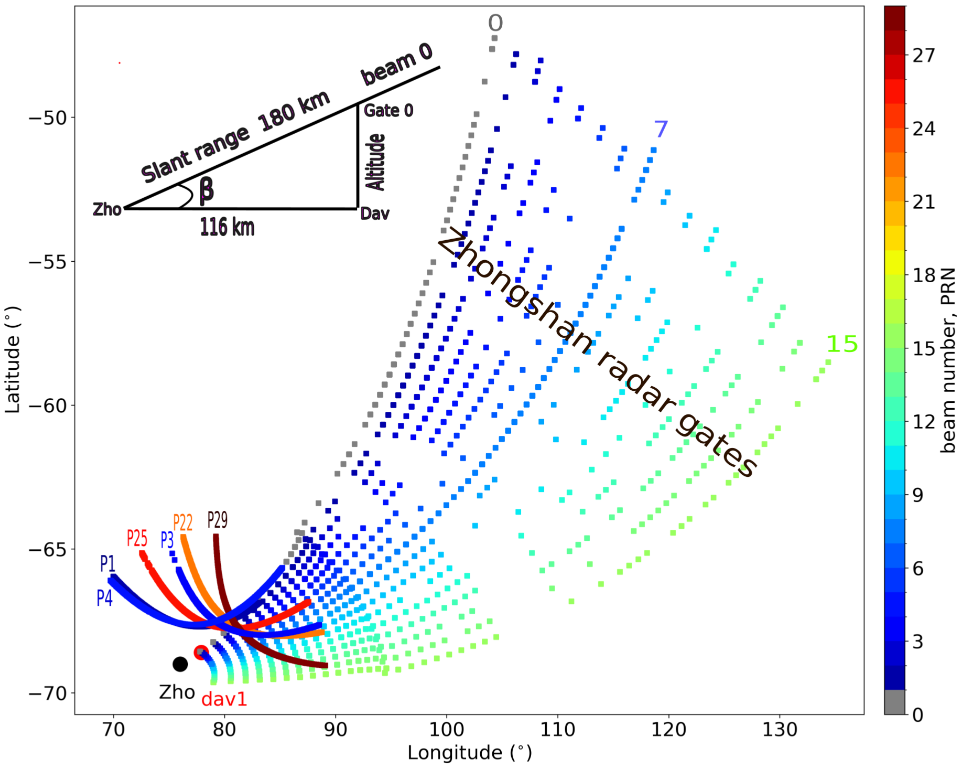

Figure 1. The geographic locations of the Zhongshan and Davis stations relative to the Ionospheric Pierce Points (IPPs) between the ground-based receiver and the satellite are shown by a black and red dot, respectively. Six Pseudo-Random Noise codes (PRNs) P1, P3, P4, P22, P25 and P29 overlapped a few gates of the first 15 beams of the Zhongshan radar during the period 08:00-22:00 UT. Coordinates of the gates of 16 beams of the Zhongshan radar, where the backscatter was available on 1 September 2019 between 19:00 and 22:00 UT, are shown in its Field Of View (FOV). Gate 0 (68.6°S, 77.8°E) at 180 km slant range of beam 0 almost coincided with the Davis station (68.6°S, 77.9°E).

2.2 Davis GPS TEC receiver

The Davis TEC receiver, located at 68.6°S, 77.9°E is one of 10 International GNSS (Global Navigation Satellite System) Service (IGS) stations in Antarctica (Xi et al., 2020). Davis station is located ~116 km northeast of Zhongshan, as illustrated in Fig. 1. The TEC in TEC unit (TECU) is derived from either the signal phase difference or from pulse travel time measurements of the orbiting satellite and geostationary signals (Otsuka et al., 2002; Rama Rao et al., 2006). To derive the vertical TEC (VTEC), the GPS TEC software developed at Boston College (Seemala and Valladares, 2011; Seemala, 2022) was used. Some assumptions were made in order to derive the VTEC. These assumptions were taken from the book by Singh and Tiwari (2022) in the chapter by Seemala (2022): the ionosphere does not change rapidly, the ionosphere and plasmasphere are horizontally stratified and spatially uniform, the ionosphere ranges between 350 and 400 km (known as the thin shell model) in order to determine the Ionospheric Pierce Point (IPP). Minimizing the standard deviation or least squares method which both rely on some assumptions, were used to estimate the Differential Code Biases (DCBs). The Optimal receiver DCB, which was used with the original dataset to estimate VTEC, was estimated by assuming that the receiver DBC is constant throughout the 24-hour time period.

Data from elevation angle ≥35° were selected to avoid the multipath effects (Cherniak and Zakharenkova, 2018a). The data resolution was 30 s. A linear least-squares fit was subtracted from the derived data to remove the trend (Ding et al., 2007). Before computing the autocorrelation, the data were smoothed using a 25-minute rolling window. Figure 1 shows the Davis station (big red dot), which supplied the raw data used to derive TEC perturbation, from the six PRNs namely P1, P3, P4, P22, P25 and P29, which can also be identified by the color.

2.3 Zhongshan SuperDARN radar

Zhongshan SuperDARN radar (69°S, 76°E) is one of more than 35 HF radars that have been installed in the mid- to polar latitudes of both the northern and southern hemispheres and operate in the frequency range between 8 and 20 MHz (Greenwald et al., 1995; Chisham et al., 2007; Nishitani et al., 2019, Zhang et al., 2024). Each of the radars has at least 16 beams with more than 1200 range gates, but some have more (Zhang et al., 2024). A full azimuth of around 53° is scanned every 1 or 2 min with an integration time of between 3 and 7 s for each beam. Each radar transmits a sequence of 7 or 8 unevenly separated pulses, where each has a length of 100 or 300 μs corresponding to a range resolution of 15 or 45 km, respectively (Nishitani et al., 2019). The Auto-Correlation Function (ACF) lags are generated by means of a sequence of pulse combinations. Backscatter power or signal-to-noise ratio in dB and spectral width in m/s are obtained by fitting a linear or quadratic function of the ACF power after applying the logarithm. Doppler line-of-sight velocity can be estimated by fitting a least-square function to the measured phase of the complex value of the ACF (Chen et al., 2022). To determine the periods of TIDs, the average backscatter received by each of the radar's beams (He et al., 2004) was used. The data were smoothed using a 25-min rolling window, because the waves in this study were of large scales, that is, their periods were greater than one hour. After smoothing the SuperDARN data, a linear detrend was done before the wave period was determined. Figure 1 shows the Zhongshan radar's FOV of 16 beams numbered from 0 (left) to 15 (right) in geographic coordinates. In this study the radar was used to get the backscatter measurements needed to identify the TID signatures (He et al., 2004). The colors on the plot indicate the number of each beam.

3. Observations

From the vertical beam of the lidar, Fig. 2 shows the sodium density profile, with a 15 s time and 45 m height resolution. Wave structures were observed on 1 September 2019 from 13:00 to 24:00 UT, corresponding to 18:00-05:00 LT of the next day, Magnetic Local Time (MLT = UT + 1.75 hours). Wavy structures of enhanced density were indicated by the contour lines where the maximum sodium density exceeded 3×10^3 cm^{-3}. Waves of different scales were clearly seen within the data. Some of these structures are the signature of passing TADs (Kirkwood and Collis, 1989). Above an altitude of 90 km wavy structures of Na layers populated the upward region up to an altitude of ~100 km. As a result, there were SSLs at around 20:00-21:30 UT above an altitude of ~92.5 km. An SSL is a layer of sodium density increased by at least twice the normal background density within several minutes (Hansen and

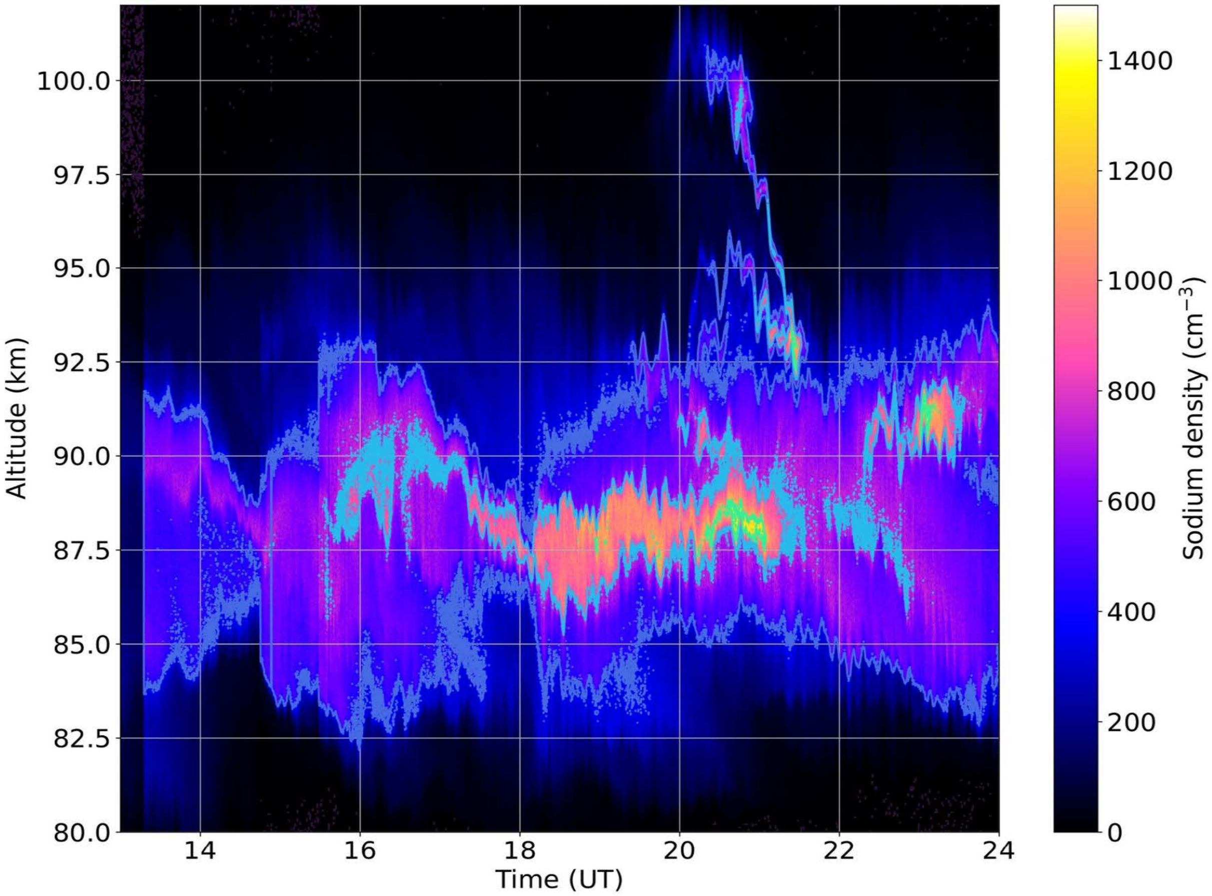

Figure 2. The TADs detected within the sodium density were derived from the lidar at Zhongshan. SSLs are obvious between 20:00 and 22:00 UT just above an altitude of 92.5 km.

Von Zahn, 1990; Qiu et al., 2021; Chen et al., 2021). For a duration of ~90 min, the sodium density was lifted upward by means of convection to form the SSL at an altitude of around 92-102 km at 19:00-21:40 UT. There were other oscillating peaks of sodium density that could be considered SSLs which were caused by the waves' propagation. These SSLs could have been formed as a result of the waves, neutral wind, electrodynamic processes and instabilities in the E-region. Signatures of the passing TADs were clearly identified within the sodium layer and SSL densities.

In order to determine the direction of wave propagation, sodium density slices at 1 km intervals at altitudes between 85 and 96 km were plotted (Kubota et al., 2006) (see Fig. 2). The used linear detrend was successful at all altitudes, except at 90 km, due to the data structure to which the linear method could not be applied. Figure 3 shows the sodium density perturbation at altitudes between 85 and 96 km. There were at least three peaks at each altitude at around 13:40, 17:00 and 20:00 UT. The maximum sodium density enhancement after removing the linear trend at 1 km intervals at altitudes between 85 and 96 km respectively, exceeded ~±50-~±200 cm^{-3}. According to the method used by Kubota et al. (2006), these enhancements are much greater than the normal background density as indicated by the sine curve fit to the data. Na number density reached saturation before and a few minutes after 16:00 UT at altitudes from 85 to 92 km with some exceptions at 86 and 89 km. They may be due to the vertical oscillations, but the data processing method could also have contributed to the saturation.

Figure 4 shows the cross-correlation between Na number density of two consecutive altitudes at 1 km vertical intervals, based on the periods 13:00-22:00 UT (a) and 16:00-24:00 UT (b) in Fig. 3. Period in panel (b) was chosen to cover the peaks that took place after 22:00 UT. Also note that peaks were not equally distributed at different altitudes. The average wavelength of the vertical oscillations at the asterisks A, B, C, D, E and F (vertical peaks) is ~4.0 km (see Fig. 4a and b). The reversed phase of Na number density fluctuations phenomenon was described by Swenson and Gardner (1998) and was evident in the stack plot of the Na number density data computed by Kubota et al. (2006). Shelton et al. (1980) also discussed the phase reversal in the SL. In the current study, there are negative and positive phase reversal oscillations. The oscillations are seen up to 85 km, but they may have also

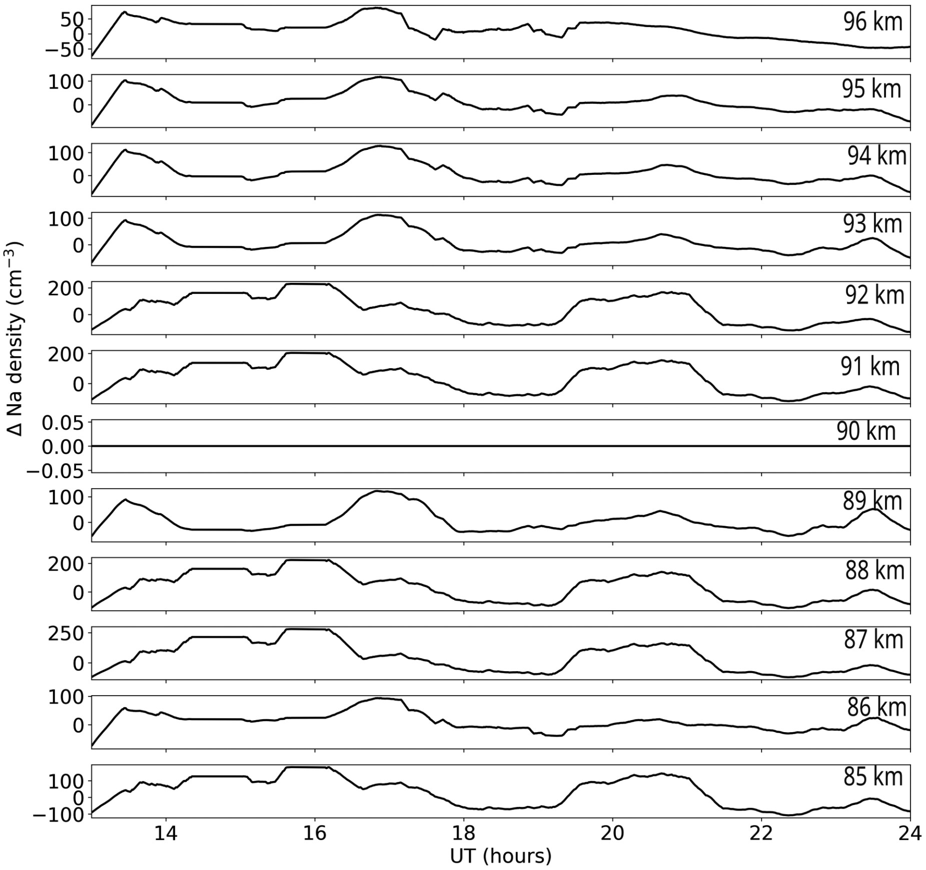

Figure 3. Sodium density perturbation at altitudes from 85 to 96 km between 13:00 and 24:00 UT. The saturation of the Na number density before and a few minutes after 16:00 UT at altitudes between 85 and 92 km with some exceptions at 86 and 89 km, are due to the vertical oscillations.

reached the lower altitudes. Negative and positive time lags show that there was upward and downward propagation of Na number density oscillations. The method described by Kubota et al. (2006) was applied to show that the oscillations slowly moved downward. Figure 4a shows that the average time lag was 7.9 min, that is, the vertical average phase velocity was 2.1 m/s. This lower value is due to the fact that there are negative and positive values. Figure 4b demonstrates that the average time lag estimated by cross-correlation was ±2.4 min, indicating that the average vertical phase velocity was ~6.9 m/s. These velocities were verified by the method of Kubota et al. (2006). A vertical wavelength, $\lambda z = 4.5$ km was calculated. Other parameters that were estimated for the vertical direction by means of the Kubota et al. (2006) method (namely sine curve fitting) are presented in Table 1. Table 1 shows that the amplitudes of the Na number density ($\Delta\rho$ Na) changed between ±10 and ±50 cm^{-3}. The vertical velocities (vz) were estimated from the values in Table 1 by means of Eq. (1):

$$v_z = \frac{\Delta z}{\Delta t} \tag{1}$$

where $\Delta z = z_{\mathrm{peak}} - z_{\mathrm{peak+1}}$ is the distance between the two consecutive vertical peaks while $\Delta t = t_{peak(z)} - t_{peak(z-\Delta z)}$ is the time lag between consecutive peaks of the wave. It may be positive (downward), negative (upward), and zero (constant vertical peak). The time lag was used to find the phase velocity, which in most cases was less than 5.5 m/s in magnitude.

The velocities presented in Table 1 are in the same range as those estimated by Kubota et al. (2006). The downward wave moved at an average speed of ~7.8 m/s and had an average period of ~8.5 min ($\mathrm{T} = \lambda z/vz$). These values are close to the above which were calculated by means of cross-correlation. Figure 4c shows peaks of very short duration between altitudes of 88 and 96 km, except at altitudes between 86 and 88 km, where the time lag was ~7.3 min. Note

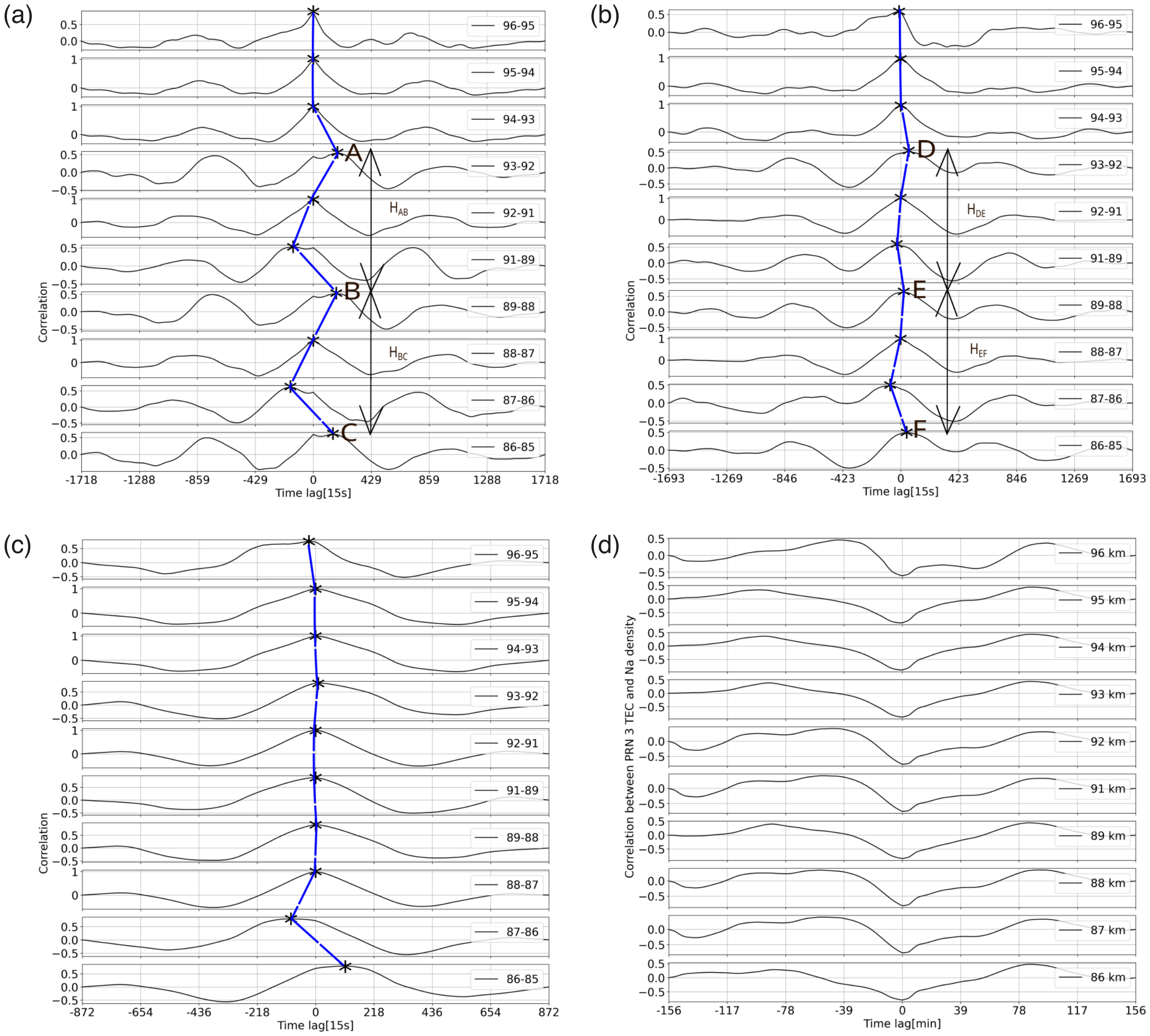

Figure 4. The cross-correlation between Na number density of two consecutive altitudes at 1 km vertical intervals, based on the periods 13:00-22:00 UT (a) and 16:00-24:00 UT (b) in Fig. 3. Vertical oscillations within sodium layers were computed for the periods 13:00-22:00 UT (a), 16:00-24:00 UT (b) and 18:00-22:00 UT (c) when the SSLs occurred. On the right-hand of each panel the pair of altitudes that were cross-correlated is indicated. H_{AB}, H_{BC}, H_{DE}, and H_{EF} show an average vertical wavelength of 4 km. The average correlation coefficient for the TEC of PRN 3 and Na number density at different altitudes, as shown in Fig. 4d was –0.7. The negative sign indicates that the GPS and lidar TIDs/TADs were out of phase.

that data for the period between 18:00 and 22:00 UT, when the SSLs occurred, were used. As will be elaborated upon in the Discussion section of this article, the instability took place at an altitude of between 84 and 88 km at around 18:45-22:00 UT. It is obvious that wave activity is stronger before 22:00 UT than after. That is why the oscillations in panel (a) are different from those in panel (b). There was multiple wave activity (TIDs) which started before 09:00 UT, as indicated by the SuperDARN radar (figure not shown).

Figure 4d shows the correlation coefficients of the TEC of PRN 3 and Na number density at different altitudes. PRN 3 TEC was used because the data were available for all three instruments at the same time period, namely 19:00-22:00 UT. Other PRNs had data for periods either before or after the availability of the lidar and SuperDARN data. The average correlation coefficient was –0.7, but generally it varied between –0.6 and –0.9 for different altitudes. The anti-correlation could be due to the fact that the TEC TIDs and Na number density AGWs were out of phase during the selected period (Smith, 1997; Fritts and Alexander, 2003). The phase difference between the vertical and horizontal components of TIDs and AGWs as well as the effects of the neutral temperature and vertical wind components could have caused the obtained negative correlation. Note that, there is a distance of ~116 km between the Zhongshan and Davis stations. An out of phase modulation was found between the AGWs and tides variances (Manson et al., 1998). There is a good correlation between the waves observed by the two instruments. Similarly, the correlation between the SuperDARN backscatter power data of beams 0-7 and Na number density was computed for different altitudes and found that there was a moderate correlation coefficient of around 0.5. It indicates that waves detected in Na number density by the lidar and those detected by the Zhongshan SuperDARN HF radar were moderately correlated. In short, these correlation coefficients indicate that the three instruments were partially observing the same waves. On the other hand the coefficients indicate that there was some interference by waves from other sources within the data of each instrument.

There were Na number density peaks that had amplitudes of between ±50 cm^{-3} and ±200 cm^{-3} (Fig. 3), but those in the sine fitted curves (Kubota et al., 2006) had amplitudes of between ±10 cm^{-3} and ±50 cm^{-3}. Based on the definition of the SSL, those large peaks in Fig. 3 could be considered as SSLs because the density variation may reach up to ten times the background density variation, as illustrated by the sine fit (Kubota et al., 2006). Based on other studies, for example, the one by Takashashi et al. (2015), those enhancements could be considered as normal SLs.

Table 1. The TAD parameters in a vertical direction estimated from the sodium density on 1 September 2019 between 16:00 and 24:00 UT. Negative time values lead to negative velocities and indicate the upward phase propagation, meaning that the motion of the waves was downward while the upward propagating waves had positive velocities.

Altitude (km)	$\Delta\rho$ Na (cm^{-3})	$t_{peak(z)}$ (hr)	$\Delta t_{peak(z)}$ (s)	v_z (m/s)
96	50	20.7	...	...
95	10	20.9	528.0	1.9
94	50	20.8	−198.0	−5.1
93	50	20.7	−383.0	−2.6
92	25	20.5	−759.0	−1.3
91	50	20.5	17.0	58.8
89	50	20.6	395	5.1
88	20	20.5	−445.0	−2.2
87	25	20.5	0.0	...
86	20	20.7	858.0	1.2
85	10	20.5	−858.0	−1.2

4. Discussions

To explain the reason behind the unusual vertical oscillations and the formation of SSLs, the presence of waves and instabilities, as well as their impact on the region are discussed. It is important to be aware of geomagnetic activity before, during and after the events described in this study.

4.1 Geomagnetic activity

The Auroral Electrojet (AE) and Polar Cap (PC) indices were used to understand the geomagnetic activity at high latitudes. Figure 5 shows the AE and PC indices between 30 August 2019 and 3 September 2019. During this time the Kp index increased from 1 to 3^+ on 30 August 2019. It reached the active levels and started to recover on 3 September 2019 when the Kp index dropped to $<2^-$. On 1 September 2019, when the waves occurred during the day, the Kp index was 4^+-5^+. The blue vertical dashed lines in the figure show the start and end of the storm. Figure 5a shows the AE indices. The AE index represents the total current density in the auroral region and can be used as a proxy for the magnitude of Joule heating rate during geomagnetic storms (Iyemori and Rao, 1996). Data for a few hours before and after the storm are also shown. There is a linear relationship between the Joule heating rate (JH) and AE, but it has been suggested that the PC index is more accurate than the AE index for the estimation of the JH (Chun et al., 1999). The AE index is derived from the northern hemisphere's instrumentation data, that is, the AE index does not reflect the magnetic activity in the southern hemisphere accurately. Fortunately, the PCS index can be

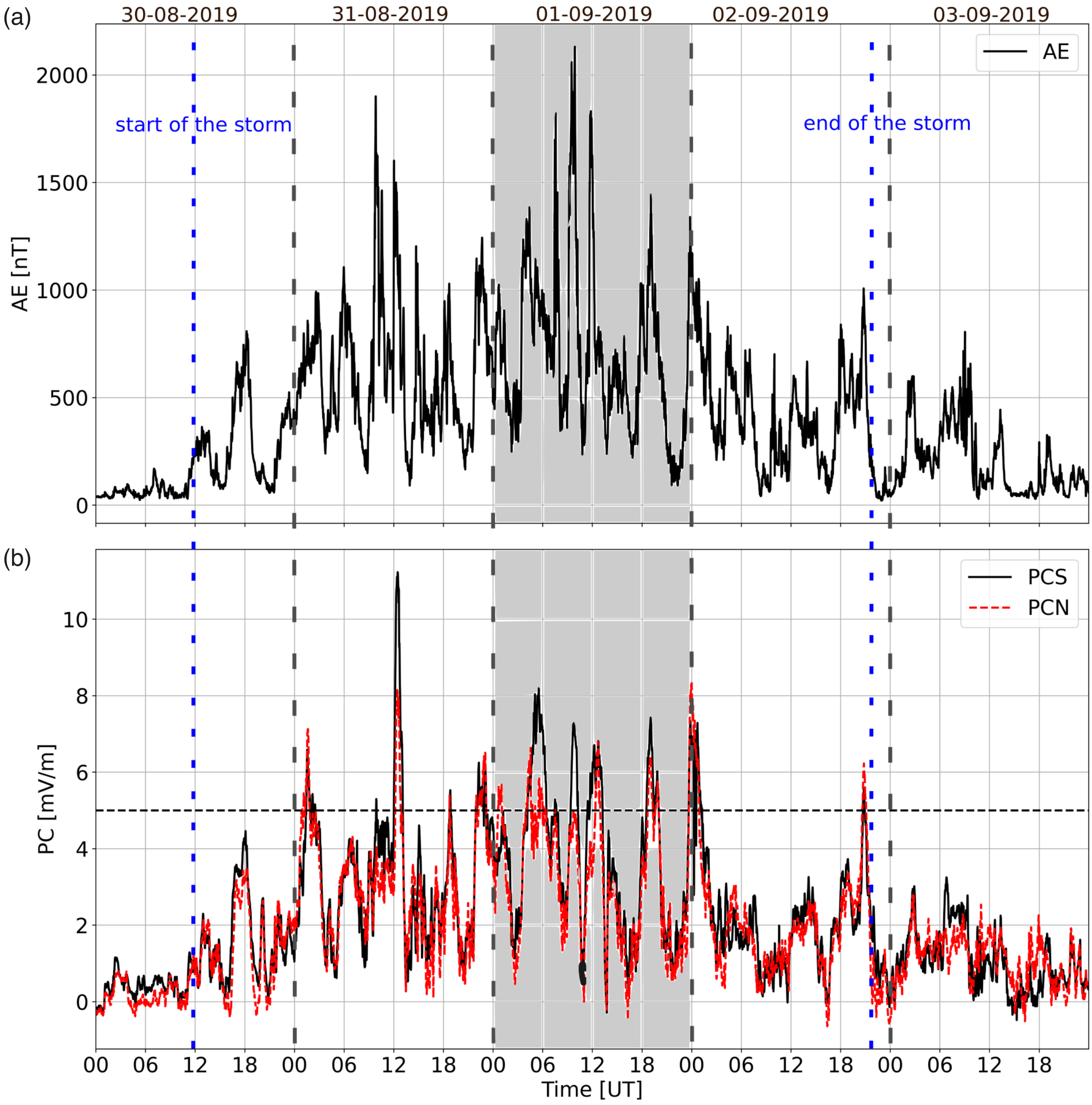

Figure 5. The geomagnetic indices with 1-min resolution: AE (a) and PC (b) indices for the period 30 August to 3 September 2019. The blue vertical dashed lines indicate the start and end time of the storm, while the black dashed line shows the end of each day in UT. There is a horizontal black dashed line in panel (b) where PC = 5 mV/m.

used to estimate the JH. Figure 5b of the figure shows both the North (N) and South (S) PC index fluctuating between ~−1 and ~12 mV/m. There are 11 and 6 peaks indicating an extreme storm during five days and on 1 September 2019, the day of the event (highlighted in grey on the figure), respectively. The PCS index at each peak was >5 mV/m for the duration of the storm. A PC index of ≥5 nT in the northern hemisphere polar cap would be equivalent to the JH of ≥~237 GW from the quadratic model developed by Chun et al. (1999).

Additional figures similar to Fig. 2 on 30 August 2019, 02 and 04 of September 2019 are presented in Section 1 of the supporting document (Figs. 1-4). There was a strong correlation between the PC/AE index and Na number density of 1-min data resolution at altitudes between 85 and 95 km during the geomagnetic storm main phase. A weak correlation was determined for the data set on 1 and 4 September 2019 (see Section 2 of the supporting document). Yuan et al. 2025 found no correlation between the nightly average Na number density and Dst index at altitudes of 80-98 km in the mid-latitudes, but a positive correlation between the two was found at altitudes above 100 km.

4.2 TIDs and AGWs

Instruments observed waves that were generated by different sources and it is not possible to determine all their characteristics due to insufficient data and instrumentation in the region. For example, TIDs are only visible in a few beams and gates of the Zhongshan radar and there are only two GPS receivers near the radar. At least three GPS receivers are needed to determine TID propagation direction. In order to estimate TID characteristics by means of cross-spectral analysis, one needs to use several beams that are separated by a given distance based on the scale of the TIDs (He et al., 2004). For this reason, AGW/TID characteristics were not investigated in detail and it is not within the scope of the current study. The analysis of the vertical oscillations of the sodium density, as well as the formation of SSLs and their possible causes, are discussed.

Figure 6 shows the TEC perturbation derived from GPS observations over Davis station. PRNs P1, P3, P4, P22, P25 and P29 passed over Zhongshan radar FOV from the 4th gate of beam 0 to the 10th gate of beams 8 and 9 (see Fig. 1) during the period 08:00-22:00 UT when TIDs were observed. PRN 29 crossed beams 0-14 at around 10:00-13:00 UT. PRNs were arranged according to the time of their initial recording in UT, that is, the time when the receiver first received a measurement from a specific satellite on 1 September 2019. Perturbations (TIDs/TADs) are assumed to be triggered by the geomagnetic storm effects within the ionosphere. Figure 6a shows that TEC of various amplitudes was derived from PRN 25. The TEC varied between ±~2 to ±~0.5 TECU during the period between 07:50 and 11:13 UT. PRN 29 in panel (b) recorded TEC of ±~1 TECU amplitude between 09:45 and 12:42 UT. A decreasing amplitude from ±~2 to ±~0.2 TECU was derived from the PRN 4 in panel (c) during the period 12:50 to 16:16 UT. PRN 1 in panel (d) showed that the derived TEC perturbation was ± ~1 TECU and sometimes reached ~2 TECU from 17:00 to 20:00 UT. Perturbation of TEC derived from the PRN 22 was nearly constant with ±~1.5 TECU between 18:16 and 21:20 UT (see panel (e)). Figure 6f shows variation in perturbation of ±~0.2-±~2 TECU between 19:00 and 22:10 UT.

The Zhongshan SuperDARN radar observed TIDs during the periods 09:00-12:00 UT (figure not shown) and 19:00-22:00 UT. Figure 7 shows the backscatter power (panel a), Doppler velocity (panel b) and spectral width (panel c) in slant range 180-800 km (gates 0-14) of beam 0 of the Zhongshan radar at 19:00-22:00 UT. The fact that TID signatures are seen in the backscatter received by gate 0 indicates that TIDs were propagating at altitudes of ~100 km and higher above the lidar and HF radar station. TIDs in beam 0 are seen as forward-slanting enhancements (indicated by forward-slanting black lines inserted manually) followed by depletions in each of the three SuperDARN products, namely backscatter power, Doppler velocity and spectral width. Similar TIDs recorded by the same instruments were reported by Hiyadutuje et al. (2022), Hiyadutuje et al. (2024a) and Hiyadutuje et al. (2024b). Forward-slanting black lines in all panels indicate that TIDs were moving away from the radar. Figure 7a shows that the backscatter perturbation was ~5-~40 dB. Figure 7b shows that the Doppler velocity fluctuated between –500 and 0 m/s, while Fig. 7c shows that the spectral width was ~0-~400 m/s. The earlier waves, between 09:00 and 12:00 UT, are shown in the backscatter power and were received by the far ranges of beam 15 of the Zhongshan HF radar, indicating that those TIDs were at a higher altitude (Senior et al., 2006).

TIDs/TADs were observed at the lowest altitude of around 100 km (in the ranges 180-600 km) away from the radar as indicated by the ray tracing (figures not shown). SSLs were observed at altitudes of between 85 and 105 km over the Zhongshan station and at around 116 km from gate 0 of beam 0 of the radar. Note that SuperDARN does not perform well during geomagnetic storms (Currie et al., 2016; Hiyadutuje et al., 2024a), implying that it is difficult

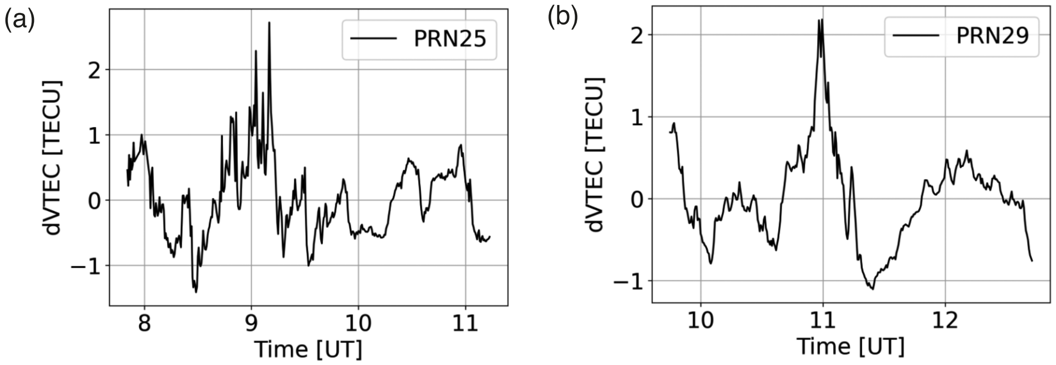

(a) dVTEC derived from PRN25

(b) dVTEC derived from PRN29

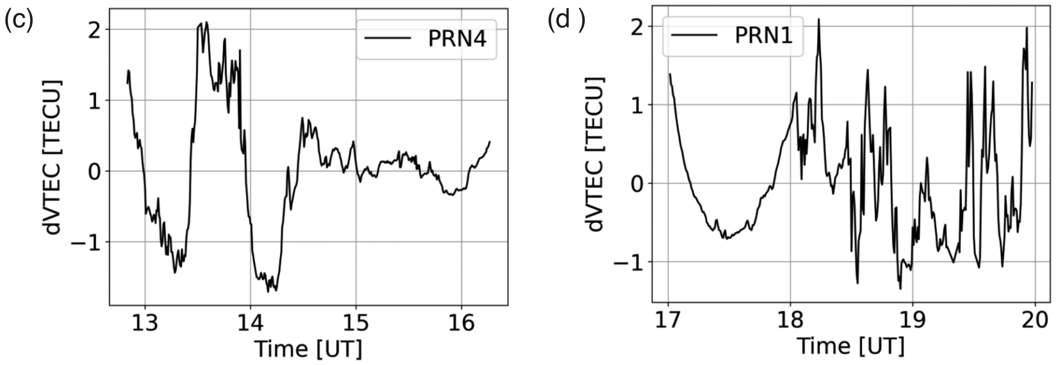

(c) dVTEC derived from PRN4

(d) dVTEC derived from PRN1

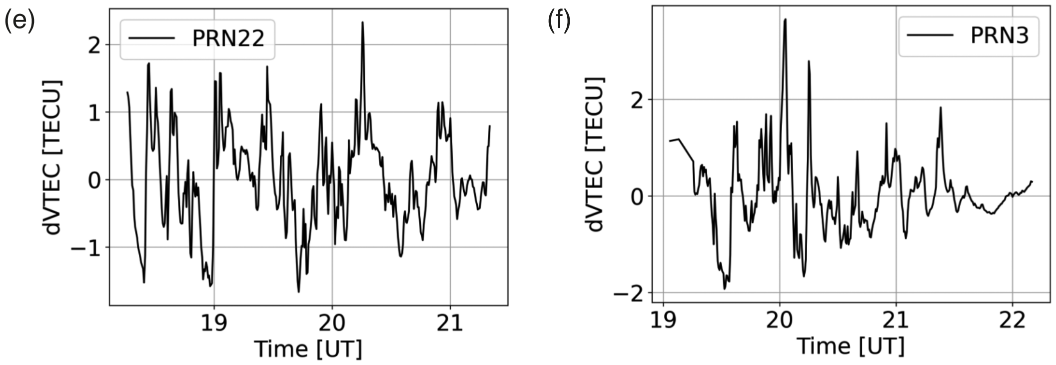

(e) dVTEC derived from PRN22

(f) dVTEC derived from PRN3

Figure 6. TEC perturbation derived from the Davis GPS receiver on 1 September 2019.

to determine when the TADs/TIDs started in Fig. 7 due to a possibility of missing data as a result of the storm. Other TADs/TIDs were observed earlier during the period 09:00-12:00 UT in the far ranges, meaning that they were traveling in the ionospheric F-region. The TIDs in the far ranges may have affected the E-region instabilities through the polarization electric field (Otsuka et al., 2007, 2009; Hiyadutuje et al., 2022, 2024a). SuperDARN slant ranges are not exactly horizontal distances, that is, they have some components of the vertical distances (altitudes) based on the hops and elevation angles (Liu et al., 2012). The closer the slant range, the lower the altitude. Those waves were seen between 180 and ~800 km slant range, meaning that waves had vertical components in the ionosphere as previously reported by Senior et al. (2006). The forward trend indicates the upward phase velocity and corresponds to the downward group velocity, meaning that their energy had a downward component. At high latitudes, Joule heating as discussed above, could be the source of these TIDs in the ionospheric E-region (Nijimbere, 2020).

Autocorrelation was done to determine the periodicity in the dataset (figure not shown). It was found that waves observed by different instruments differed. The computation of other characteristics of the TIDs/AGWs is beyond the

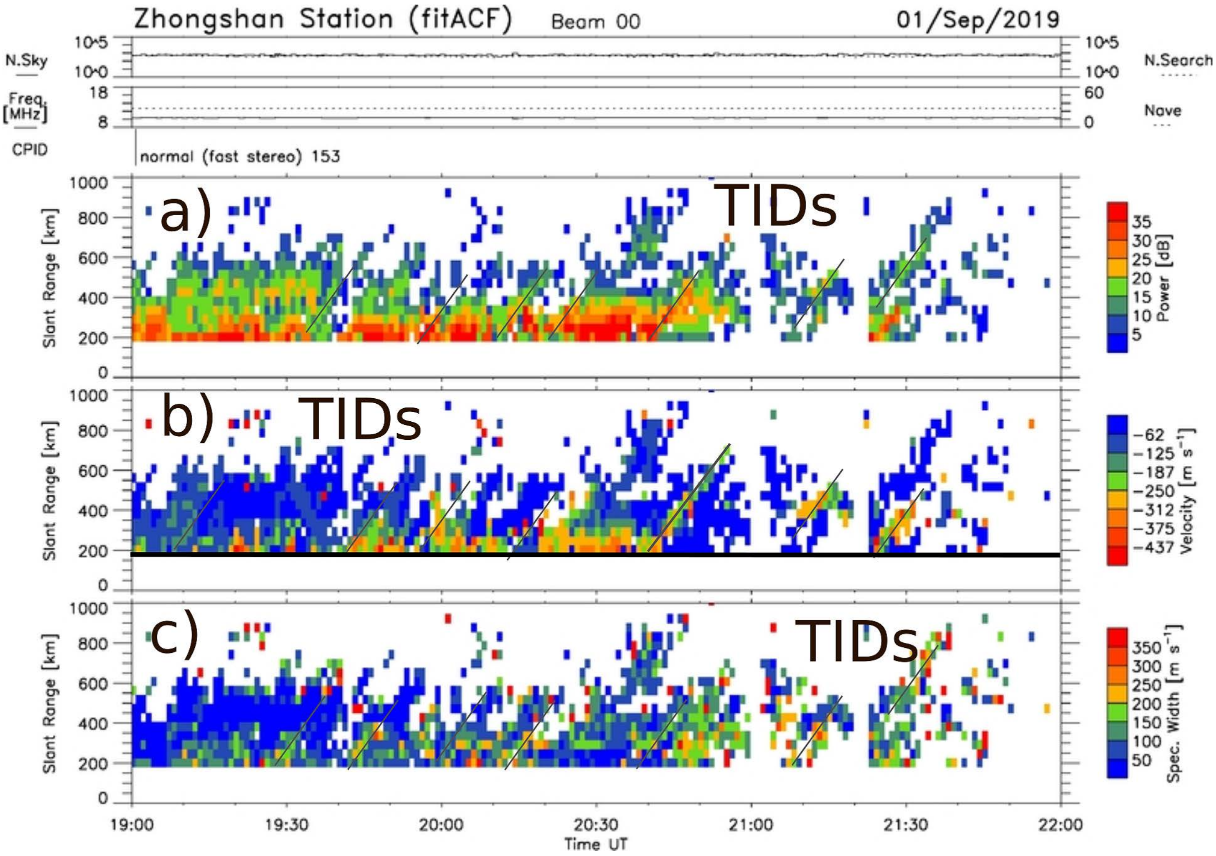

Figure 7. Traveling ionospheric disturbances observed by the Zhongshan HF radar on 1 September 2019 between 19:00 and 22:00 UT. Panels (a), (b) and (c) show the backscatter power, Doppler velocity and spectral width, respectively.

scope of this study and as mentioned earlier, the data were not sufficient, probably due to the effects of geomagnetic activity on the radar and a scarcity of other instrumentation in the region.

The neutral temperature and neutral wind at altitudes between 80 and 105 km were examined. Figure 8a shows the neutral temperature between 150 and 230 K plotted with contour lines. The neutral wind data in Figs. 8b and c exhibit wave structures. These wave structures and the alternation between enhancement (see black dashed lines) and decrease in neutral temperature indicate a downward phase velocity, hence the group velocity of the AGWs was upward, indicating that their source was below an altitude of ~90 km. On the other hand, in Fig. 7 SuperDARN ray tracing showed that the TID/TAD backscatter echoes in the slant ranges 180-800 km came from an altitude of ~100 km. In this context, if the TIDs were horizontal then the oscillations would have been caused by the TID vertical amplitudes (in km) when the AGWs were moving upward. The downward TADs interfered with upward AGWs to generate the observed sodium density oscillations (see Fig. 4) at altitudes between 80 and 105 km. The reduction of the wavelength at altitudes between 86 and 90 km obtained by means of the method of Kubota et al. (2006) is an indication of wave breaking and/or the destructive mutual interference of downward TADs and upward AGWs. The same method showed the forward trend of the peaks (figure not shown) which indicates that the group energy of the resultant oscillating waves moved downward, meaning that the downward components, that is, TIDs/TADs slightly dominated.

It was found that the zonal neutral wind showed a downward propagating phase structure. It was westward for the duration of around 8 hours at an altitude above 90 km (Chen et al., 2021). The meridional neutral wind also showed a downward phase. Figure 8 shows the same downward trend observed in this study as in the one observed in Fig. 8 by Chen et al. (2021). Downward phase structures were also obvious in the neutral temperature.

Wavy structures in the sodium density can be generated by multiple mechanisms, such as TADs, AGWs, neutral wind, and some instabilities. Sodium density caused by either the ion recombination processes or was directly carried by substances that contain sodium by means of waves and/or neutral wind. At high latitudes, the sporadic E (Es) layer's vertical drift is governed by the neutral wind ($\mathbf{U}$), convectional electric field ($\mathbf{E}$), particle interactions, Earth's magnetic field (**B**), ambipolar diffusion and the force of gravity (Kirkwood and Von Zahn, 1991; Kirkwood and Nilsson, 2000; Chen et al., 2021; Hiyadutuje et al., 2024b). When SSLs are secondary features of metal ions from the *Es*-layers or if SSLs are generated through the recombination of ions (Kirkwood and Von Zahn, 1991; Kirkwood and Nilsson, 2000; Chen et al., 2021), the dynamics strongly depend on the electric field.

When SSLs are generated directly by the sodium layers and are not formed by the ion recombination processes, which is likely the case in this study, then the neutral wind and neutral temperature as well as the acceleration due to gravity would play an important role in the dynamics of neutral particles. Note that downward TADs or upward AGWs would also contribute to the dynamics. Myrabø et al. (1987) suggested that the convective instability, also known as convective wave breakdown advected by the neutral wind, could generate the SSL (Sherman and She, 2006). SLs that took place between 13:00 and 24:00 UT (Fig. 2) could have been caused by the action of downward TADs, upward AGWs and the neutral wind in the region (Sherman and She, 2006). Myrabø et al. (1987) proposed that ripples such as those in Fig. 2 are due to the superposed short and long wavelength of the interfered waves. Ripples are also due to the dynamic instability which is associated with Kelvin-Helmholtz billows (Taylor and Hapgood, 1990) or wave structures that are not easily differentiated from the instability (Li et al., 2017). In the next subsection, convection and dynamic instabilities are proposed as the mechanisms behind the formation of SSLs. The instabilities may also have participated in the vertical oscillation of the sodium density layers against the downward propagating TADs/TIDs.

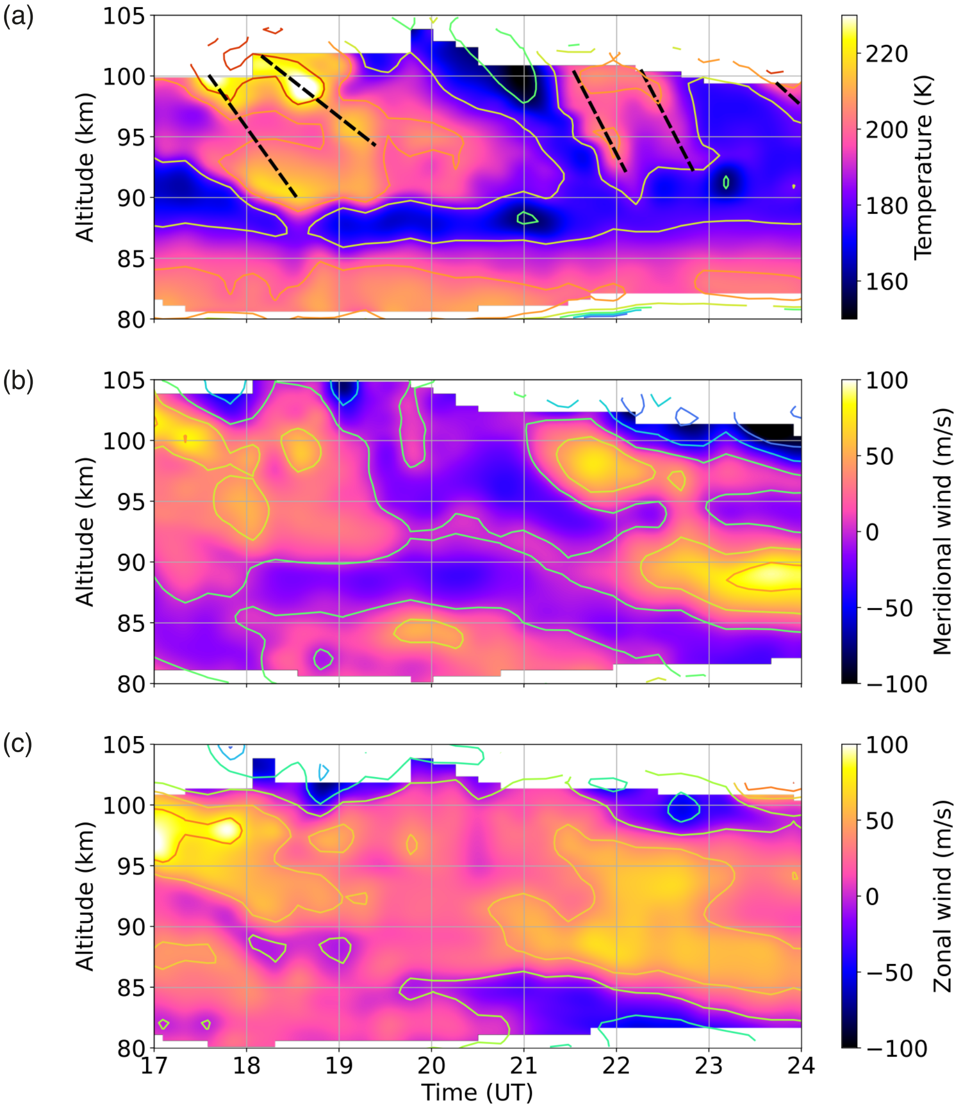

Figure 8. Neutral temperature (a), meridional wind (b), and zonal wind (c) at Zhongshan on 1 September 2019 between 17:00 and 24:00 UT. AGWs are seen in the repeated neutral temperature perturbation shown in the wavy structures of the contour lines.

4.3 Convective instability

The atmospheric dynamic instability that causes convective instability can be demonstrated using the Richardson number (Ri), expressed by the following (Sherman and She, 2006). First, the square of buoyancy, also known as Brunt-Väisälä frequency, N^2 was estimated:

$$N^2 = \frac{g}{T}\left(\frac{\partial T}{\partial z} + \frac{g}{C_p}\right). \tag{2}$$

It characterizes the atmospheric convective stability associated with temperature inversion. Next, the square magnitude of vertical shear of horizontal neutral wind, S^2 was estimated as:

$$S^2 = \left(\frac{\partial U}{\partial z}\right)^2 + \left(\frac{\partial V}{\partial z}\right)^2. \tag{3}$$

Finally, the Ri can be estimated by means of the Eqs. (2) and (3) as:

$$Ri = \frac{N^2}{S^2}. \tag{4}$$

Note that g, T, Cp, U and V are the acceleration due to gravity, neutral temperature, specific heat at constant pressure, neutral zonal and meridional wind velocities (see Fig. 8), respectively.

Figure 9a is similar to Fig. 2, but shows sodium density between 16:00 and 24:00 UT. Figure 9b shows the Ri values estimated by means of the Eq. (4) during the period 16:00-24:00 UT. The purpose of the comparison was to see the region of SSLs in (a) and the possible location of the instabilities in (b). The red and blue trends in this panel show the maxima of the sodium main and sporadic sodium layer, respectively. Dynamic and convective instabilities occur when $0 < Ri < 0.25$ and $Ri < 0$, respectively (Fritts and Alexander, 2003; Sherman and She, 2006; Nappo, 2012). The signature of the upward AGWs are present as the enhanced values of Ri which are indicated by the backward

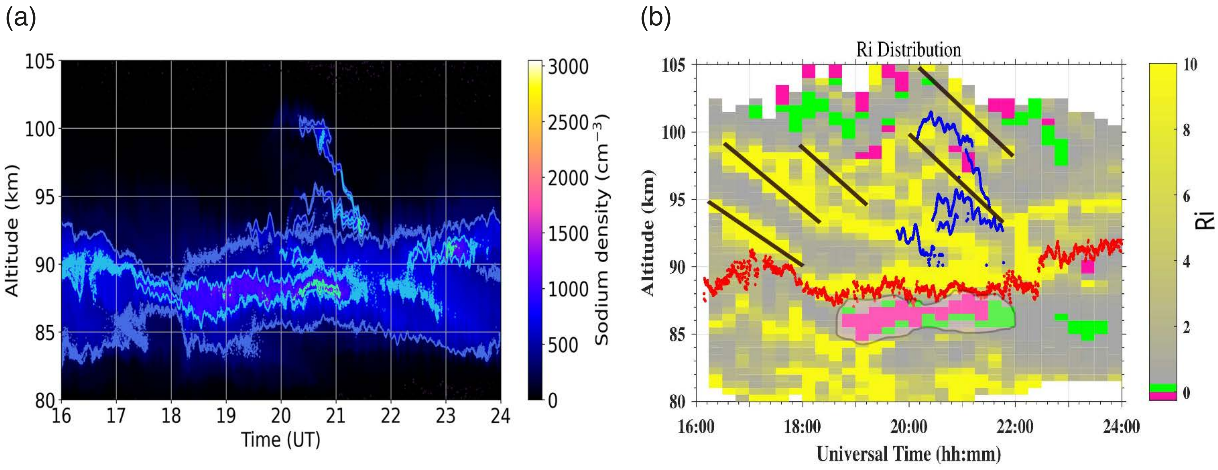

Figure 9. (a) shows the same figure as Fig. 2 at 16:00-24:00 UT. (b) Shows the estimated Ri values for 1 September 2019 at 16:00-24:00 UT in the altitudes between 80 and 105 km. The red trend indicates the mesospheric main sodium layer, while the blue line shows the SSLs observed in Fig. 2 superimposed on the estimated Ri values. The bins in pink and green show the distribution of convective and dynamic instabilities, respectively. The long-lived instability (encircled by the gray line) at an altitude between 84 and 88 km at 18:45-22:00 UT is the source of the SSLs.

oblique lines. Nappo (2012) suggested that AGWs could be generated by turbulence through exchange of kinetic energy. In our case, it is possible that the upward AGWs were generated by the convective (Sato, 1992) and dynamic instabilities. Other studies reported that AGWs could be generated in the lower part of the atmosphere by numerous sources. They can also be reflected from the ground and move upward. Instabilities occurred at different altitudes and times, but the long-lived one occurred at an altitude between 84 and 88 km at around 18:45-22:00 UT. The neutral temperature in this region was below 180 K and the meridional wind was southerly (see Fig. 8). The convective instability is more likely to be the primary source of the observed SSLs in Fig. 2 due to the upward convectional displacement of the already existing sodium density layers.

5. Conclusions

Unusual vertical oscillations in sodium density layers with some wave structures were observed by means of a lidar during a geomagnetic storm. SSLs were also observed just after the start of the instabilities that lasted for about 2.5 hours. SuperDARN HF radar and Na lidar, both located at the Zhongshan station in Antarctica were used to investigate these structures. A nearby GPS receiver station at Davis ~116 km northeast of Zhongshan was also used to investigate the ionospheric perturbations. The findings of this study can be summarized as follows:

1) The average vertical wavelength, speed and period of the vertical waves were ~3.0-4.5 km, ~7.8 m/s, and ~7.3-8.5 min, respectively.
2) There was a good anti-correlation of 0.6-0.9 between the TEC perturbation of PRN 3, derived from a GPS receiver at Davis station, and Na number density perturbations at different altitudes. The anti-correlation indicates that the correlated waves were out of phase. A moderate correlation was found between the Zhongshan SuperDARN HF radar backscatter power and the same Na number density data. This correlation indicated that GPS, lidar and SuperDARN radar observed varying wave activity in the region coming from both common and non-common sources. A strong correlation between the PC/AE index and Na number density is found during a few hours of the main phase of the storm, but for the rest of the storm time there was a weak correlation.
3) Sodium density at the bottom of the ionospheric E-region was enhanced periodically due to the wave propagation resulting in the formation of SLs of enhanced density at altitudes between 80 and 90 km. It has been suggested that the vertically oscillating layers are caused by mutual interference of the downward propagating TADs and upward propagating AGWs. TIDs/TADs were possibly triggered by an electrodynamic process like Joule heating. The SSLs between 20:00 and 21:30 UT were generated by the convective and dynamic instabilities at an altitude between 84 and 88 km and were modulated by neutral wind dynamic processes.

Data availability statement. The lidar data can be accessed via the Chinese National Polar Scientific Data center (https://en.pric.org.cn/).
GNSS data are available at https://www.unavco.org/data/gps-gnss/file-server/file-server-access-examples.html or https://cddis.nasa.gov/Data_and_Derived_Products/GNSS/GNSS_data_and_product_archive.html.
SuperDARN radar data at Zhongshan station belong to the Chinese Meridian Project and Chinese National Polar Scientific Data Center (https://en.pric.org.cn/). The Zhongshan HF radar raw data of the event on 1 September 2019 can be downloaded from Super Dual Auroral Radar Network (2022). The SuperDARN raw data can also be found at the BAS SuperDARN data mirror (https://www.bas.ac.uk/project/superdarn/#data). Alternatively, the data can be found at https://data.meridianproject.ac.cn/.
The PC Magnetic Index data are available at https://pcindex.org/. The AE index can be downloaded from the OMINWeb page at https://omniweb.gsfc.nasa.gov/ow_min.html.

Acknowledgments. Financial assistance (grant number: 144832) towards this research was received from the South African National Research Foundation (SANRF). Opinions expressed and conclusions arrived at are those of the authors and are not to be attributed to the SANRF. X.C. Chen received grants (grant numbers: 42130210 and 42120104003) from the National Natural Science Foundation of China (NNSFC).
Dr. Gopi Seemala provided the GPS software which was used to derive TEC (http://seemala.blogspot.com/).
Everybody who contributed to this work is acknowledged. Especially, Dr. Stefan Lotz for his input on the proposition of using the cross correlation method. The normal ways of tracing the AGW propagation direction in the sodium density

were not working in this study due to the complexity of the data (with vertical oscillations present).
The GNSS receiver networks, International GNSS Service (IGS) and SuperDARN community made the satellite and radar data freely available. SuperDARN is a collection of scientific HF radars funded by national scientific funding agencies of Australia, Canada, China, France, Italy, Japan, Norway, South Africa, the United Kingdom and the United States of America. The Zhongshan sodium lidar operation was supported by the Chinese Antarctic Expedition. The authors acknowledge the use of data from the Chinese Meridian Project.

References

Avakyan, S. (2008). Physics of the solar-terrestrial coupling: Results, problems, and new approaches, Geomag. Aeronomy, 48, 417-424, doi:10.1134/S0016793208040014.

Bruinsma, S. L. and J. M. Forbes (2007). Global observation of traveling atmospheric disturbances (TADs) in the thermosphere, Geophys. Res. Lett., 34, L14103, doi:10.1029/2007GL030243.

Bruinsma, S. L and J. M. Forbes (2009). Properties of traveling atmospheric disturbances (TADs) inferred from CHAMP accelerometer observations, Adv. Space Res., 43, 369-376, doi:10.1016/j.asr.2008.10.031.

Cai, X., T. Yuan and J. V. Eccles (2017). A numerical investigation on tidal and gravity wave contributions to the summer time Na variations in the midlatitude E region. Journal of Geophysical Research: Space Physics, 122, 10,577-10,595, doi:10.1002/2016JA023764.

Chen, X., W. Huang, C. Ban, M. J. Kosch et al. (2021). Dynamic properties of a sporadic sodium layer revealed by observations over Zhongshan, Antarctica: A case study, J. Geophys. Res-Space, 126, e2021JA029787, doi:10.1029/2021JA029787.

Chen, X., J. Liu, M. J. Kosch, Z. Hu et al. (2022). Simultaneous observations of a sporadic E layer by Digisonde and SuperDARN HF radars at Zhongshan, Antarctica, J. Geophys. Res-Space, 127, e2021JA029921, doi:10.1029/2021JA029921.

Cherniak, I. and I. Zakharenkova (2018a). Ionospheric total electron content response to the great American solar eclipse of 21 August 2017, Geophys. Res. Lett., 45, 1199-1208, doi:10.1002/2017GL075989.

Cherniak, I. and I. Zakharenkova (2018b). Large-scale traveling ionospheric disturbances origin and propagation: Case study of the December 2015 geomagnetic storm, Space Weather, 16, 1377-1395, doi:10.1029/2018SW001869.

Chisham, G., M. Lester, S. Millan, M. Freeman et al. (2007). A decade of the Super Dual Auroral Radar Network (SuperDARN): scientific achievements, new techniques and future directions, Surv. Geophys., 28, 33-109, doi:10.1007/s10712-007-9017-8.

Chun, F. K., D. J. Knipp, M. G. McHarg, G. Lu et al. (1999). Polar cap index as a proxy for hemispheric Joule heating, Geophys. Res. Lett., 26, 1101-1104, doi:10.1029/1999GL900196.

Currie, J., C. Waters, F. Menk, M. Sciffer et al. (2016). SuperDARN backscatter during intense, geomagnetic storms, Radio Sci., 51, 814-825, doi:10.1002/2016RS005960.

Ding, F., W. Wan, B. Ning and M. Wang (2007). Large-scale traveling ionospheric disturbances observed by GPS total electron content during the magnetic storm of 29-30 October 2003, J. Geophys. Res-Space, 112, A06309, doi:10.1029/2006JA012013.

Fritts, D. C. and M. J. Alexander (2003). Gravity wave dynamics and effects in the middle atmosphere, Rev. Geophys., 41, 1003, doi:10.1029/2001RG000106.

Gardner, C. S. and J. D. Shelton (1985). Density response of neutral atmospheric layers to gravity wave perturbations, J. Geophys. Res-Space, 90, 1745-1754, doi:10.1029/JA090iA02p01745.

Greenwald, R., K. Baker, J. Dudeney, M. Pinnock et al. (1995). DARN/SuperDARN: A global view of the dynamics of high-latitude convection, Space Sci. Rev., 71, 761-796, doi:10.1007/BF00751350.

Hansen, G. and U. Von Zahn (1990). Sudden sodium layers in polar latitudes, J. Atmos. Terr. Phys., 52, 585-608, doi:10.1016/0021-9169(90)90055-R.

He, L. S., P. Dyson, M. Parkinson and W. Wan (2004). Studies of medium scale travelling ionospheric disturbances, using TIGER SuperDARN radar sea echo observations, Ann. Geophys., 22, 4077-4088, doi:10.5194/angeo-22-4077-2004.

Hecht, J. H., C. Fricke Begemann, R. L. Walterscheid, J. Höffner (2000). Observations of the breakdown of an atmospheric gravity wave near the cold summer mesopause at 54N, Geophys. Res. Lett., 27, 879-882, doi:10.1029/1999GL010792.

Hecht, J., R. Walterscheid, M. P. Hickey and S. J. Franke (2001). Climatology and modeling of quasi-monochromatic atmospheric gravity waves observed over Urbana Illinois, J. Geophys. Res-Atmos., 106, 5181-5195, doi:10.1029/2000JD900722.

Heinselman, C., J. Thayer and B. Watkins (1998). A high-latitude observation of sporadic sodium and sporadic E-layer formation, Geophys. Res. Lett., 25, 3059-3062, doi:10.1029/98GL02215.

Hiyadutuje, A., M. J. Kosch and J. A. Stephenson (2022). First observations of E-region near range echoes partially modulated by F-region traveling ionospheric disturbances observed by the same SuperDARN HF radar, J. Geophys. Res-Space, 127, e2021JA030157, doi:10.1029/2021JA030157.

Hiyadutuje, A., J. B. Habarulema, M. J. Kosch, X. Chen et al. (2024a). Simultaneous occurrence of traveling ionospheric disturbances, Farley Buneman and gradient drift instabilities observed by the Zhongshan SuperDARN HF radar, J. Geophys. Res-Space, 129, e2023JA031367, doi:10.1029/2023JA031367.

Hiyadutuje, A., M. J. Kosch, J. B. Habarulema, X. Chen et al. (2024b). Observation of sporadic E layer altitude partially modulated by the traveling ionospheric disturbances at high latitudes over Zhongshan station, J. Atmos. Terr. Phys., 265, 106377, doi:10.1016/j.jastp.2024.106377.

Hocke, K. and K. Schlegel (1996). A review of atmospheric gravity waves and travelling ionospheric disturbances: 1982-1995, Ann. Geophys., 14, 917-940, doi:10.1007/s00585-996-0917-6.

Hunsucker, R. D. (1982). Atmospheric gravity waves generated in the high-latitude ionosphere: A review, Rev. Geophys., 20, 293-315, doi:10.1029/RG020i002p00293.

Iyemori, T. and D. Rao (1996). Decay of the Dst field of geomagnetic disturbance after substorm onset and its implication to storm-substorm relation, Ann. Geophys., 14, 608-618, doi:10.1007/s00585-996-0608-3.

Kirkwood, S. and P. Collis (1989). Gravity wave generation of simultaneous auroral sporadic-E layers and sudden neutral sodium layers, J. Atmos. Terr. Phys., 51, 259-269, doi:10.1016/0021-9169(89)90077-9.

Kirkwood, S. and U. Von Zahn (1991). On the role of auroral electric fields in the formation of low altitude sporadic-E and sudden sodium layers, J. Atmos. Terr. Phys., 53, 389-407, doi:10.1016/0021-9169(91)90034-5.

Kirkwood, S. and H. Nilsson (2000). High-latitude sporadic-E and other thin layers – the role of magnetospheric electric fields, Space Sci. Rev., 91, 579-613, doi:10.1023/A:1005241931650.

Krueger, D. A., C. Y. She and T. Yuan (2015). Retrieving mesopause temperature and line-of-sight wind from full-diurnal-cycle Na lidar observations, Appl. Optics, 54, 9469-9489, doi:10.1364/AO.54.009469.

Kubota, M., S. Kawamura, M. Abo, Y. Koizumi et al. (2006). A fast-propagating, large-scale atmospheric gravity wave observed in the WAVE2004 campaign, J. Geophys. Res-Atmos., 111, D21110, doi:10.1029/2005JD006788.

Li, J., T. Li, S. Dou, X. Fang et al. (2017). Characteristics of ripple structures revealed in OH airglow images, J. Geophys. Res-Space, 122, 3748-3759, doi:10.1002/2016JA023538.

Liu, E., H. Hu, R. Liu, Z. Wu et al. (2012). An adjusted location model for SuperDARN backscatter echoes, Ann. Geophys., 30, 1769-1779, doi:10.5194/angeo-30-1769-2012.

Liu, J. Y., H. F. Tsai and T. K. Jung (1996). Total electron content obtained by using the global positioning system, Terr. Atmos. Ocean. Sci, 7, 107-117, doi:10.3319/TAO.1996.7.1.107(A).

Manson, A. H., C. E. Meek and G. E. Hall (1998). Correlations of gravity waves and tides in the mesosphere over Saskatoon, J. Atmos. Terr. Phys., 60, 1089-1107, doi:10.1016/S1364-6826(98)00059-5.

Munro, G. (1950). Travelling disturbances in the ionosphere, P. R. Soc-Math. Phys. Sc., 202, 208-223, doi:10.1098/rspa.1950.0095.

Myrabø, H., C. Deehr, R. Viereck and K. Henriksen (1987). Polar mesopause gravity wave activity in the sodium and hydroxyl night airglow, J. Geophys. Res-Space, 92, 2527-2534, doi:10.1029/JA092iA03p02527.

Nappo, C. J. (2012). Gravity wave instability and turbulence, Int. Geophys., 102, 117-157, doi:10.1016/B978-0-12-385223-6.00005-7.

Super Dual Auroral Radar Network (2022). SuperDARN 2019 RAWACF, Federated Research Data Repository, doi:10.20383/102.0558.

Nijimbere, V. (2020). A mathematical model for the numerical simulations of traveling ionospheric disturbances/atmospheric gravity waves generated by the Joule heating, Phys. Fluids, 32, 076602, doi:10.1063/5.0008649.

Nishtani, N., J. M. Ruohoniemi, M. Lester, J. B. H. Baker et al. (2019). Review of the accomplishments of mid-latitude Super Dual Auroral Radar Network (SuperDARN) HF radars, P. Earth Planet. Sc., 6, 1-57, doi:10.1186/s40645-019-0270-5.

Nomura, A., T. Kano, Y. Iwasaka, H. Fukunishi et al. (1987). Lidar observations of the mesospheric sodium layer at Syowa Station, Antarctica, Geophys. Res. Lett., 14, 700-703, doi:10.1029/GL014i007p00700.

Otsuka, Y., T. Ogawa, A. Saito, T. Tsugawa et al. (2002). A new technique for mapping of total electron content using GPS network in Japan, Earth Planets Space, 54, 63-70, doi:10.1186/BF03352422.

Otsuka, Y., F. Onoma, K. Shiokawa, T. Ogawa et al. (2007). Simultaneous observations of nighttime medium-scale traveling ionospheric disturbances and E region field-aligned irregularities at midlatitude, J. Geophys. Res-Space, 112, A06317, doi:10.1029/2005JA011548.

Otsuka, Y., K. Shiokawa, T. Ogawa, T. Yokoyama et al. (2009). Spatial relationship of nighttime medium-scale traveling ionospheric disturbances and F region field-aligned irregularities observed with two spaced all-sky airglow imagers and the middle and upper atmosphere radar, J. Geophys. Res-Space, 114, A05302, doi:10.1029/2008JA013902.

Plane, J. M. C., W. Feng and E. C. M. Dawkins (2015). The mesosphere and metals: Chemistry and changes, Chem. Rev., 115, 4497-4541, doi:10.1021/cr500501m.

Qiu, S., Y. Tang, M. Jia, X. Xue et al. (2016). A review of latitudinal characteristics of sporadic sodium layers, including new results from the Chinese Meridian Project, Earth Sci. Rev., 162, 83-106, doi:10.1016/j.earscirev.2016.07.004.

Qiu, S., N. Wang, W. Soon, G. Lu et al. (2021). The sporadic sodium layer: a possible tracer for the conjunction between the upper and lower atmospheres, Atmos. Chem. Phys., 21, 11927-11940, doi:10.5194/acp-21-11927-2021.

Rama Rao, P., S. G. Krishna, K. Niranjan and D. Prasad (2006). Temporal and spatial variations in TEC using simultaneous measurements from the Indian GPS network of receivers during the low solar activity period of 2004-2005, Ann. Geophys., 24, 3279-3292, doi:10.5194/angeo-24-3279-2006.

Richmond, A. (1978). Gravity wave generation, propagation, and dissipation in the thermosphere, J. Geophys. Res-Space, 83, 4131-4145, doi:10.1029/JA083iA09p04131.

Richmond, A. (1979). Thermospheric heating in a magnetic storm: Dynamic transport of energy from high to low latitudes, J. Geophys. Res-Space, 84, 5259-5266, doi:10.1029/JA084iA09p05259.

Roble, R., A. Richmond, W. Oliver and R. Harper (1978). Ionospheric effects of the gravity wave launched by the September 18, 1974, sudden commencement, J. Geophys. Res-Space, 83, 999-1009, doi:10.1029/JA083iA03p00999.

Sato, K. (1992). Vertical wind disturbances in the afternoon of mid-summer revealed by the MU radar, Geophys. Res. Lett., 19, 1943-1946, doi:10.1029/92GL02244.

Seemala, G. and C. Valladares (2011). Statistics of total electron content depletions observed over the South American continent for the year 2008, Radio Sci., 46, 1-14, doi:10.1029/2011RS004722.

Seemala, G. K. (2022). Estimation of ionospheric total electron content (TEC) from GNSS observations, Adv. Space Res. (A. K. Sing and S. Tiwari), 63-84, doi:10.1016/B978-0-323-99262-6.00022-5.

Senior, A., M. Kosch, T. K. Yeoman, M. Rietveld et al. (2006). Effects of high-latitude atmospheric gravity wave disturbances on artificial HF radar backscatter, Ann. Geophys., 24, 2347-2361, doi:10.5194/angeo-24-2347-2006.

Shelton, J. D., C. S. Gardner and C. F. Sechrist Jr (1980). Density response of the mesospheric sodium layer to gravity wave perturbations, Geophys. Res. Lett., 7, 1069-1072, doi:10.1029/GL007i012p01069.

Sherman, J. P. and C. Y. She (2006). Seasonal variation of mesopause region wind shears, convective and dynamic instabilities above Fort Collins, CO: A statistical study, J. Atmos. Terr. Phys., 68, 1061-1074, doi:10.1016/j.jastp.2006.01.011.

Shinbori, A., Y. Otsuka, T. Sori, M. Nishioka et al. (2022). Electromagnetic conjugacy of ionospheric disturbances after the 2022 Hunga Tonga-Hunga Ha'apai volcanic eruption as seen in GNSS-TEC and SuperDARN Hokkaido pair of radars observations, Earth Planets Space, 74, 1-17, doi:10.1186/s40623-022-01665-8.

Smith, A. K. (1997). Stationary planetary waves in upper mesospheric winds, J. Atmos. Sci., 54, 2129-2145, doi:10.1175/1520-0469(1997)054<2129:SPWIUM>2.0.CO;2.

Singh, A. K. and S. Tiwari (2022). Atmospheric Remote Sensing: Principles and Applications, Elsevier, 63-84, ISBN: 978-0-323-99262-6.

Snively, J. B. and V. P. Pasko (2003). Breaking of thunderstorm-generated gravity waves as a source of short-period ducted waves at mesopause altitudes, Geophys. Res. Lett., 30, 2254, doi:10.1029/2003GL018436.

Swenson, G. R. and C. S. Gardner (1998). Analytical models for the responses of the mesospheric OH* and Na layers to atmospheric gravity waves, J. Geophys. Res-Atmos., 103, 6271-6294, doi:10.1029/97JD02985.

Takahashi, T., S. Nozawa, T. T. Tsuda, Y. Ogawa et al. (2015). A case study on generation mechanisms of a sporadic sodium layer above Tromsø (69.6°N) during a night of high auroral activity, Ann. Geophys., 33, 941-953, doi:10.5194/angeo-33-941-2015.

Taylor, M. J. and M. Hapgood (1990). On the origin of ripple-type wave structure in the OH nightglow emission, Planet. Space Sci., 38, 1421-1430, doi:10.1016/0032-0633(90)90117-9.

Von Zahn, U., P. Von der Gathen and G. Hansen (1987). Forced release of sodium from upper atmospheric dust particles, Geophys. Res. Lett., 14, 76-79, doi:10.1029/GL014i001p00076.

Williams, P., G. Crowley, K. Schlegel, T. Viridi et al. (1988). The generation and propagation of atmospheric gravity waves observed during the worldwide Atmospheric Gravity-wave Study (WAGS), J. Atmos. Terr. Phys., 50, 323-338, doi:10.1016/0021-9169(88)90018-9.

Xi, H., H. Jiang, J. An, Z. Wang et al. (2020). Spatial and temporal variations of polar ionospheric total electron content over nearly thirteen years, Sensors, 20, 540, doi:10.3390/s20020540.

Yiğit, E., P. K. Knížová, K. Georgieva and W. Ward (2016). A review of vertical coupling in the atmosphere – ionosphere system: Effects of waves, sudden stratospheric warmings, space weather, and of solar activity, J. Atmos. Terr. Phys., 141, 1-12, doi:10.1016/j.jastp.2016.02.011.

Yu, B., X. Xue, G. Lu, C. L. Kuo et al. (2017). The enhancement of neutral metal Na layer above thunderstorms, Geophys. Res. Lett., 44, 9555-9563, doi:10.1002/2017GL074977.

Yuan, T., P. D. Pautet and M. J. Taylor (2025). Midlatitude mesosphere and lower thermosphere variations during the extreme gannon geomagnetic storm in May 2024, Front. Astr. Space Sci., 11, 1516222, doi:10.3389/fspas.2024.1516222.

Zhang, J., A. Lan, J. Yan, X. Deng et al. (2024). Development of the Chinese dual auroral radar network and preliminary results, Space Weather, 22, e2024SW004131, doi:10.1029/2024SW004131.

***CORRESPONDING AUTHOR: Alicreance HIYADUTUJE**,
South African National Space Agency (SANSA), Hermanus, South Africa
e-mail: hiyadutujea@yahoo.fr